




## From stress concentrations between inclusions to probability of breakage: A two-dimensional peridynamic study of particle-embedded materials

Xavier Frank <sup>\*</sup>, Komlanvi Lampoh , and Jean-Yves Delenne   
IATE, Univ. Montpellier, INRAE, Institut Agro, F-34060 Montpellier, France



(Received 3 April 2023; accepted 28 August 2023; published 21 September 2023)

Particle-embedded materials consist of a dispersed phase of particles in a sticking matrix. We used a bond-based peridynamics method to investigate their elastic properties, rupture, and probability of failure. We performed an extensive two-dimensional parametric study where particles are disk-shaped inclusions diluted into a pore-filling matrix. Both particle and matrix are considered to be brittle elastic with a perfectly bonded interface. The inclusion volume fraction  $\varphi$  and the inclusion matrix toughness ratio  $\beta$  ( $\beta \geq 1$ ) were varied from 0.254–0.754 (jamming point) and 1.5–100.0, respectively. A total of 5000 uniaxial tensile tests up to failure were performed. We showed that the Halpin-Tsai model fits well all Young elastic moduli even for nearly in-contact particles. The stress distribution strongly depends on  $\varphi$  and  $\beta$ . As the highest stresses (at the origin of crack nucleation) occur between neighboring particles, we analyzed the average stress in gaps. We found that, regardless of the particle volume fraction, the yield stress is a power law of a grain-scaled stress concentration factor. We also investigated the probability of failure of the samples. We found that whatever  $\varphi$  and  $\beta$ , this probability follows a classical Weibull law. Finally, we showed that Weibull modulus, normalized by its value for infinitely rigid particles, is inversely proportional to a function of the stress concentration factor.

DOI: [10.1103/PhysRevE.108.034903](https://doi.org/10.1103/PhysRevE.108.034903)

### I. INTRODUCTION

Particle-embedded materials can be found in many applications in engineering [1], food products [2], pharmaceutical [3], or in geological structures such as sandstone or granite [4]. The variability of their strength and yield stress is important for the design of industrial products [5], analysis of food texture [6], and strength of concrete [7].

In the simplest cases, Particle-embedded materials can be seen as two-phase materials composed of a dispersed collection of particles embedded in a continuous percolating phase. Similarly to fluid suspensions, the bulk mechanical properties depend to first order on the particle volume fraction. The highest particle volume fractions correspond to the so-called cemented granular material, for example, sandstone or wheat endosperm (composed of starch granules glued together by a gluten matrix) [8]. For this typical microstructure, the contact between the particles plays an important role as it concentrates the stresses and can potentially lead to asymmetrical behavior between tension and compression, or be at the origin of dissipative interactions at contact [9,10].

In contrast, particle-embedded composites have been extensively studied from an experimental point of view [11–13]. Most theoretical models (i.e., Halpin-Tsai, Mori-Tanaka, self-consistent) used to predict their elastic properties assumes a diluted phase of particles. However, although the elastic properties are well predicted, the accuracy of the models generally decreases with increasing particle volume fraction. In addition, in this limit, the yield stress and probability of

failure cannot be predicted solely by considering the volume of phases and the disordered structure of the solid suspension should be considered. To do so, numerical simulation is a powerful tool to take into account complex microstructures. For example, Laubie *et al.* [14] provide a systematic parametric study of stress transmission and failure of two-dimensional (2D) porous materials in which the pore spacial distribution is controlled by a disorder parameter.

The numerical modeling of the failure of heterogeneous materials remains a challenging issue. One major challenge is to take into account the time-evolving discontinuities induced by crack nucleation and propagation. Finite-element methods have been enriched to take into account the occurrence of fractures. As examples, popular approaches are XFEM method [15], cohesive zone [16], phase field [17]. Nevertheless, due to the general use of unstructured meshes, complex rupture models, or heavy remeshing procedures [18], these approaches remain highly time consuming. On the contrary, regular lattice-based approaches are easy to parallelize and offer a versatile framework for the simulation of heterogeneous materials with complex spacial phase distribution. For example, the lattice elements method (LEM) relies on a triangular mesh of the domain in which each lattice bond is connected to a pair of material points and is characterized by stiffness and a yield force [9]. This simple approach has been proven to be very efficient for the simulation of cementitious granular materials including a pore phase [8,19]. However, the small connectivity of the material points, which are only bonded to the nearest neighbors may lead to undesired meshing effects. Although the theoretical underpinnings are different [20], the peridynamic (PD) approach generalizes the LEM by considering connected bonds beyond the nearest neighbors. Using

\*xavier.frank@inrae.fr

this nonlocal framework meshing effects nearly vanish, and the mechanical behavior and dynamics of crack propagation can be addressed in a reasonable time.

In this work, by means of the peridynamics method we investigate the Young modulus, yield stress, and probability of failure of disk-shaped particle-embedded composites. We varied the matrix-inclusion stiffness ratio and the inclusion dilution over a wide range. In each case, we performed 100 replicates with different random draws of particle positions.

We first introduce the outline of the bond-based peridynamics model. A discrete element method (DEM) procedure is employed to generate sample structures and map disk-shaped inclusions in the peridynamics domain. Sample series of different particle volume fractions are generated by varying the particle radius. We describe the parametric study performed on 5000 tensile tests on samples with different stiffness ratios and particle volume fractions. The data from this extensive parametric study are then used to study the statistics of the mechanical properties in relation to the microstructure of the composites.

## II. BOND-BASED PERIDYNAMICS

The peridynamic (PD) approach [20] is an alternative theoretical framework to classical continuum mechanics. Unlike continuum mechanics based on partial differential equations, PD is a nonlocal approach based on an integrodifferential formulation. In the PD, material points are assumed to interact remotely up to a so-called horizon distance  $h$  for which the interactions become negligible.

In this study, we used the bond-based peridynamics (BBPD) approach [21], which relies on pairwise interactions. The BBPD provides a simple and efficient framework for the simulation of brittle elastic materials and is capable to upscale the stress distribution inside highly heterogeneous materials [22]. Furthermore, the BBPD has been used successfully to simulate crack initiation and propagation for theoretical issues such as crack branching [23,24] or applications to the rupture of various types of heterogeneous materials (concrete [25] or wood [26]).

The simulations are performed using a parallelized in-house BBPD code developed by Frank *et al.* [10,22]. Samples are first discretized in material points  $i = 1, \dots, N$  of positions  $\mathbf{x}_i = (x_i, z_i)$  regularly distributed on a grid of space step  $\delta x$ . This configuration is chosen as the initial time reference ( $t = 0$ ). At time  $t$ , all points  $i$  will be at position  $\mathbf{x}_i + \mathbf{u}_i$ , where  $\mathbf{u}_i$  is the displacement of point  $i$ . From Newton's second law, we get for a node  $i$ :

$$m_i \ddot{\mathbf{u}}_i(t) = \sum_{\mathcal{H}(\mathbf{x}_i)} k_{ij} s(\boldsymbol{\xi}_{ij}, \boldsymbol{\eta}_{ij}) \frac{\boldsymbol{\xi}_{ij} + \boldsymbol{\eta}_{ij}}{\|\boldsymbol{\xi}_{ij} + \boldsymbol{\eta}_{ij}\|} + \mathbf{b}_i(t), \quad (1)$$

where  $\mathcal{H}(\mathbf{x}_i)$  is the set of bonds  $\boldsymbol{\xi}_{ij} = \mathbf{x}_j - \mathbf{x}_i$  connecting  $\mathbf{x}_i$  to its neighbors  $\mathbf{x}_j$  within a circular domain of size  $h$  called the horizon ( $\|\mathbf{x}_j - \mathbf{x}_i\| \leq h$ ),  $m_i$  is the mass of the point  $i$ ,  $\mathbf{u}_i(t)$  is its displacement,  $\boldsymbol{\eta}_{ij} = \mathbf{u}_j - \mathbf{u}_i$  is the deformation of  $\boldsymbol{\xi}_{ij}$ , and  $\mathbf{b}_i(t)$  is a body force applied to the node  $i$  (Fig. 1). The factor  $k_{ij}$  is the stiffness of the bond connecting  $i$  and  $j$  and its

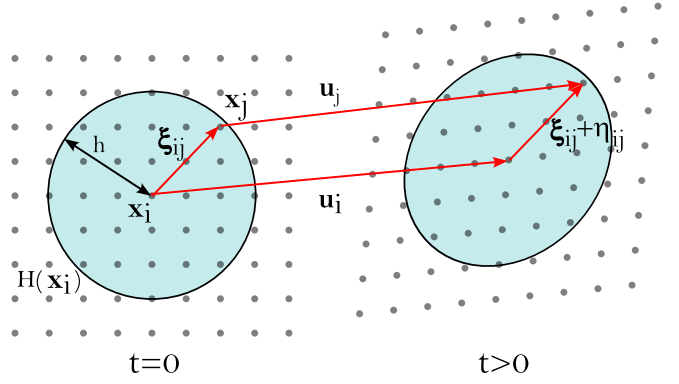


FIG. 1. Schematic view of the discretized peridynamic approach. Left: reference state ( $t = 0$ ). A material point  $\mathbf{x}_i$  is chosen, the neighborhood  $\mathcal{H}(\mathbf{x}_i)$  of  $\mathbf{x}_i$ , the horizon  $h$  and a point within the neighborhood  $\mathbf{x}_j$  are shown. The bond between  $\mathbf{x}_i$  and  $\mathbf{x}_j$  is  $\boldsymbol{\xi}_{ij}$ . Right: state after strain ( $t > 0$ ). The displacement of both  $\mathbf{x}_i$  and  $\mathbf{x}_j$  are  $\mathbf{u}_i$  and  $\mathbf{u}_j$ , respectively. The deformation of  $\boldsymbol{\xi}_{ij}$  is  $\boldsymbol{\eta}_{ij}$ .

elongation can be obtained using

$$s(\boldsymbol{\xi}_{ij}, \boldsymbol{\eta}_{ij}) = \frac{\|\boldsymbol{\xi}_{ij} + \boldsymbol{\eta}_{ij}\| - \|\boldsymbol{\xi}_{ij}\|}{\|\boldsymbol{\xi}_{ij}\|}. \quad (2)$$

With this model, a solid material before failure behaves as an elastic material and the bond stiffness  $k_{ij}$  can be deduced from an effective Young's modulus  $E^{\lambda(i,j)}$  [24] following

$$k_{ij} = \frac{6\delta x^4 E^{\lambda(i,j)}}{\pi h^3 (1 - \nu)}, \quad (3)$$

where  $\lambda(i, j)$  is the index of the type of the bond between  $i$  and  $j$ , and  $\nu = 1/3$  is the Poisson ratio. When  $i$  and  $j$  belong to the same phase,  $E^{\lambda(i,j)}$  refers to Young's modulus of this phase. On the other hand, when  $i$  and  $j$  belong to different phases, the bond between  $i$  and  $j$  is an interface bond and its modulus  $E^{\lambda(i,j)}$  must be defined as an additional material parameter. Note that Eq. (3) is valid for any system of springs uniformly distributed on a regular grid and whatever the range of the neighborhood [25].

In order to simulate the opening of cracks, we assume that bonds break when they reach an elongation exceeding a critical value  $s_0^{\lambda(i,j)}$ . The force exerted by a bond after failure is then definitely set to 0. The critical elongation can be deduced from a fracture energy  $G_c^{\lambda(i,j)}$  using

$$s_0^{\lambda(i,j)} = \sqrt{\frac{4\pi G_c^{\lambda(i,j)}}{9E^{\lambda(i,j)}h}}. \quad (4)$$

The toughness  $K_c^{\lambda(i,j)}$  of the material can be deduced from  $K_c^{\lambda(i,j)} = \sqrt{E^{\lambda(i,j)}G_c^{\lambda(i,j)}}$ .

Finally, it should be noted that it is not equivalent to calculating the phase volume from the number of nodes or links. In the following, we will use the latter definition. Further technical details about the numerical approach can be obtained in Ref. [10].

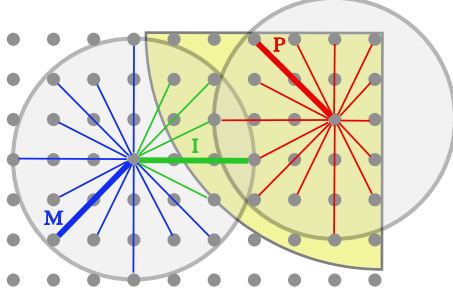


FIG. 2. Schematic view of the material properties allocated to bonds. A quarter particle is shown in yellow at the top right, the matrix is everywhere else. Examples of particle bonds (P), matrix bonds (M), and interface (I), are shown in red, blue, and green, respectively. To guide the eyes, two examples of neighborhoods (light gray disks) are drawn.

### III. NUMERICAL EXPERIMENTS

In this study, we choose to focus on 2D composites composed of disk-shaped particles embedded in a matrix (Fig. 2). The mechanical behavior of each phase is characterized by its Young modulus and toughness:  $(E^p, K_c^p)$  for the particle bonds (shown in red in Fig. 2) and  $(E^m, K_c^m)$  for the matrix bonds (in blue in Fig. 2). For particle-matrix interface bonds  $(E^i, K_c^i)$  shown in green (Fig. 2) we set  $E^i = E^m$  and  $K_c^i = K_c^m$ .

By this definition, the contrast of toughness between particles and matrix is controlled by a single dimensionless parameter

$$\beta = \frac{K_c^p}{K_c^m} = \frac{E^p}{E^m}. \quad (5)$$

Note that the same result holds for the fracture energy ratio.

Denoting  $s_0^p$  and  $s_0^m$  the critical elongation of particles and matrix, respectively, Eqs. (4) and (5), yields

$$s_0^p = s_0^m = s_0. \quad (6)$$

As the mechanical behavior is brittle elastic, it follows that both particles and matrix exhibit the same value of rupture strain but with different yield stress as

$$\sigma_Y^p = \beta \sigma_Y^m. \quad (7)$$

where  $\sigma_Y^p$  and  $\sigma_Y^m$  are the yield stress in tension for particle and matrix phase, respectively.

To build the samples we rely on the following procedure:

(1) The first step is to simulate granular packings of disk particles. We chose a uniform distribution of particle sizes with a ratio of 2 between the largest and smallest diameters. This slight polydispersity prevents particles from local crystallization and limits long-range ordering [Fig. 3(a)]. The particles are initially distributed on a triangular grid and then compacted without friction using a discrete element method (DEM) code [27]. Specific boundary conditions are used to obtain samples with an aspect ratio of approximately 2.

(2) In order to obtain different solid fractions of particles, we consider a shrink parameter  $\alpha$ , which is used to scale the particle size [Fig. 3(c)]. In this paper, this value of  $\alpha$  will be chosen according to targeted values of the particle fraction  $\varphi^t$ .

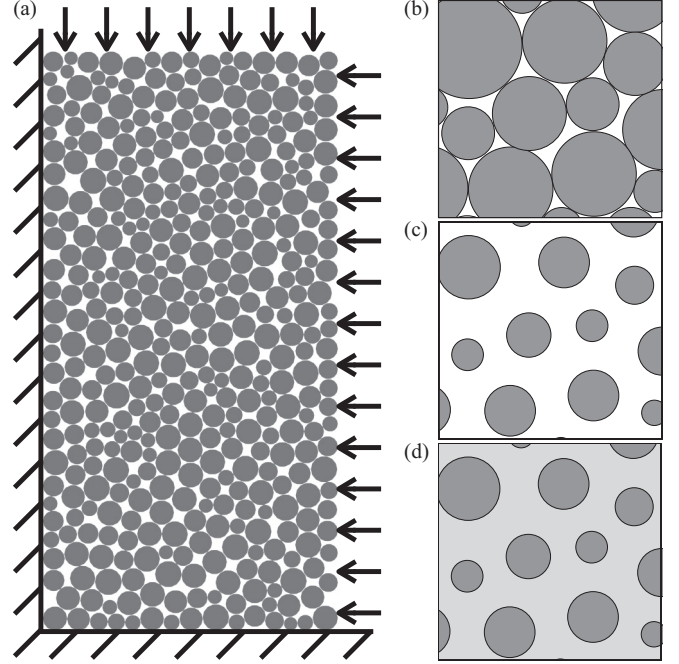


FIG. 3. Sample building procedure. (a) Boundary conditions. (b) Granular sample after compaction. (c) Granular sample after particle shrinking. (d) Final microstructure with particles (in dark gray) embedded into a matrix (in light gray).

It is worth noting that, unlike classical Monte Carlo procedures, this shrinkage method makes it possible to control the disorder that results here mainly from particle polydispersity.

(3) Peridynamics samples are then obtained from the discretization of the DEM packings. Due to the DEM procedure, the ratio of sample height to width is not perfectly equal to 2. For this reason, we used a rectilinear grid of material points of 512 in width and approximately 1024 points in height. With this procedure, we obtain biphasic samples constituted by material points representing both disk particles and matrix filling the pores [Fig. 3(d)]. For each bond, a stiffness  $k$  and a critical elongation  $s_0$  are attributed according to the phases of two nodes connected by the bond.

For all simulations, we used a horizon  $h/\delta x = 3$ , which is a good compromise between the meshing effort and the anisotropy of elastic properties (less than 5%) [28]. This value of  $h/\delta$  corresponds to a connectivity of 28 bonds per material point (in the bulk) and leads to more than  $14 \times 10^6$  bond elements per sample. Due to rasterization effects, we computed peridynamics samples' particle solid fraction using  $\varphi = N_p/N_{tot}$ , where  $N_p$  is the number of bonds in the particle phase and  $N_{tot}$  the total number of bonds. As we have considered that the interface bonds behave mechanically like the matrix bonds, we have associated the volume of the interface bonds with that of the matrix. For this reason,  $\varphi$  computed for  $\alpha = 1$  is slightly lower than the particle solid fraction of the original DEM packing.

We performed an extensive parametric study in which we varied  $\varphi$  and  $\beta$  parameters. We considered five values of  $\varphi = 0.254, 0.396, 0.530, 0.631$ , and  $\varphi = \varphi^c = 0.754$  corresponding to the case of particles in contact. Regarding  $\beta$ , ten values ranged from 1.5–100.0 were considered. For each couple

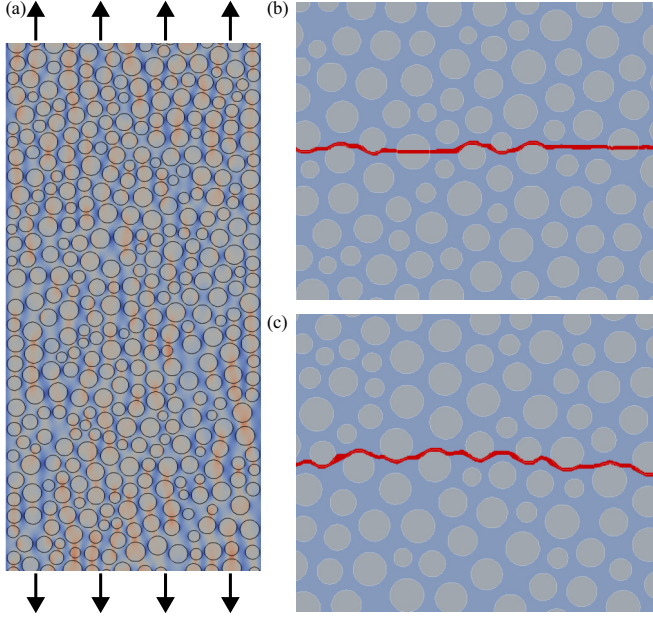


FIG. 4. (a) Example of numerical tensile test for  $\varphi = 0.631$  and  $\beta = 4.0$  showing  $\sigma_{zz}$  stress field component before failure (the color gradient ranges from dark blue for  $\sigma_{zz} = 0$  to red for  $\sigma_{zz}$  close to its maximum value). (b) and (c) shows magnifications of typical crack patterns (for  $\varphi = 0.396$ ) for toughness ratio  $\beta = 2.0$  and  $\beta = 10.0$ , respectively.

( $\varphi, \beta$ ) in the parametric space, 100 uniaxial tensile tests until rupture (Fig. 4) were performed using randomly generated configurations. The total number of mechanical tests equals thus 5000.

All tests were performed in nearly quasistatic conditions by applying opposite displacements to both the bottom and upper boundaries of the sample. The loading rate is taken sufficiently low to be able to damp the elastic waves using a small viscous force applied through the body force term [Eq. (1)]. More details about this procedure can be found in Ref. [10].

Each sample was tested under traction until complete failure. In many applications, it is interesting to determine the conditions under which inclusions are damaged [29–31]. Typical crack patterns are shown in Figs. 4(b) and 4(c) for two values of  $\beta$ . In this figure, we see that there is competition for the crack between crossing and bypassing the inclusions. It is interesting to note that at low  $\beta$  ( $\beta > 1$ ) there is a coexistence of broken and bypassed particles. In the case of the failure of a two-layered material, He and Hutchinson [32] showed theoretically that both the toughness ratio and crack angle of incidence govern the fracture path. Depending on  $\beta$  two regimes can be identified. At low  $\beta$ , the crack can cross particles. On the contrary above a critical value  $\beta_c$  (between 3 and 4), no particles are damaged. Interestingly,  $\beta_c$  is close to the theoretical value of 3.85 obtained for a disk inclusion [31,33]. In the specific case of Fig. 4(b) cracks both cross or bypass particles depending on their angle of incidence when impinging matrix-particle interfaces.

Figure 5 shows examples of the dimensionless stress  $\sigma/\sigma_Y^m$  as a function of the normalized strain  $\epsilon/s_0^m$  for four values of the toughness ratio  $\beta$  (with  $\varphi = 0.530$ ). All the samples

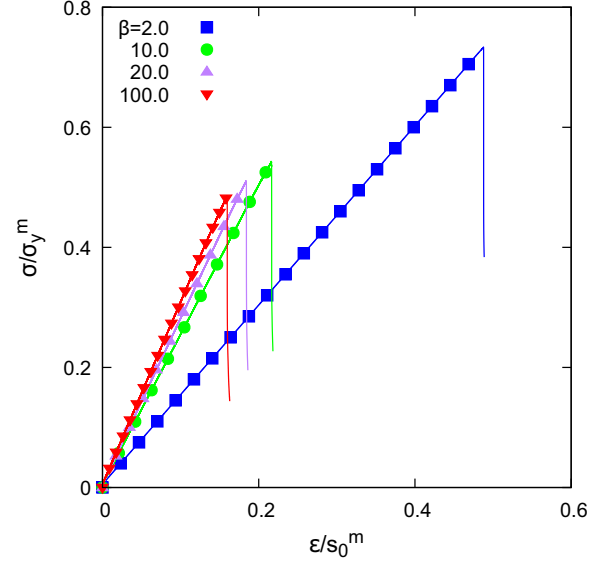


FIG. 5. Typical stress-strain curves for  $\varphi = 0.530$  and various values of  $\beta$ . The stress  $\sigma$  is normalized by the yield stress of the matrix  $\sigma_Y^m$  and the strain  $\epsilon$  is normalized by the critical elongation of the matrix  $s_0^m$ .

exhibit an elastic-brittle behavior with a well-defined slope corresponding to the normalized Young modulus  $E/E^m$  and a maximum value corresponding to the critical stress  $\sigma_Y/\sigma_Y^m$ . We find that Young's modulus increases with particle stiffness but the critical stress tends to decrease as the particles generate higher local stress concentrations.

## IV. RESULTS AND DISCUSSION

### A. Elasticity

One major interest in particle-reinforced materials is that their elastic properties can be tuned through the particle solid fraction and possibly the stiffness of the particles. Figure 6 (points) shows  $E/E^m$  as a function of  $\beta$  for different particle fractions  $\varphi$ . For each  $\varphi$  the Young modulus increases almost linearly at the beginning then level off toward the case of infinitely rigid inclusions. We also note that the error bars are very small except for high values of  $\beta$  and  $\varphi$ .

Various empirical or semiempirical micromechanics approaches were proposed to model the effective modulus of multiphase elastic materials [34,35]. In particular, these models are valid for a dilute phase of particles in a continuous matrix. However, they fail to predict with good accuracy the case of high particle solid fractions since the interfaces between particles lead to strong heterogeneities in stress concentration. For this reason, we need to account for the microstructure of the packing. For this reason, in this study, we used the semiempirical approach of Halpin-Tsai (H-T), which includes a single fitting parameter  $\zeta$  capable to describe the structural effect of the packing (Fig. 6):

$$\frac{E}{E^m} = \frac{1 + \zeta \omega \varphi}{1 - \omega \varphi} \quad (8a)$$

$$\omega = \frac{\beta - 1}{\beta + \zeta}, \quad (8b)$$

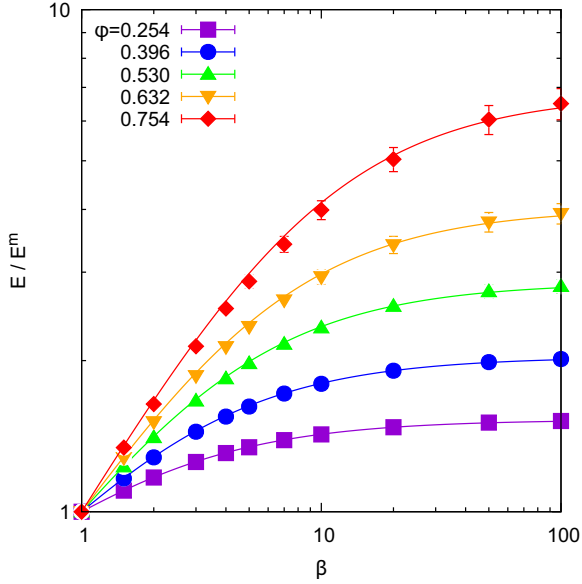


FIG. 6. Average values of samples elastic moduli  $E$  normalized by the matrix modulus as a function of  $\beta$ . Error bars display standard deviation and solid lines Halpin-Tsai prediction [Eq. (8)].

where  $\zeta$  is the so-called reinforcing efficiency (also called shape factor), which depends on the geometrical characteristics of the particles and their packing arrangement. Note that  $\omega = 0$  for a homogenous material ( $\beta = 1$ ),  $\omega = 1$  for perfectly rigid inclusions ( $\beta = \infty$ ) and  $\omega = -1/\zeta$  for holes ( $\beta = 0$ ).

The H-T model is based upon the theoretical self-consistent model developed by Hill [35] and has been successfully used to describe with very good accuracy the elastic properties of composites at high particle solid fraction [36]. It is worth noting that  $\zeta \rightarrow 0$  and  $\zeta \rightarrow +\infty$  are two limit cases that reduce to the classical inverse rule of mixture and to the rule of mixture, respectively.

$\zeta$  does not necessarily evolve in a monotonic way according to  $\varphi$ . In our case, limited to high particle load, we found

$$\zeta = 0.53 + \left(\frac{\varphi}{\varphi^c}\right)^{3.25} \quad (9)$$

with a coefficient of determination  $R^2 = 0.99$  and where  $\varphi^c \simeq 0.76$ . This result is consistent with Affdl and Kardos [36], which shows that H-T underestimates experimental values for high-volume fractions of filler. In the same vein, some authors have proposed empirical laws to take into account the deviation from the diluted case thanks to  $\varphi$  parameter [37].

### B. Stress transmission

In a heterogeneous elastic material, the elastic contrast between phases leads to local stress concentrations, which are at the origin of crack nucleation. As the stress transmission is more efficient through stiff phases, for particle-enriched composites (with  $\beta > 1$ ) stress concentrations are expected in the vicinity of particles. The case of a disk-shaped inclusion in an infinite matrix submitted to a uniaxial vertical stress  $\sigma$  was

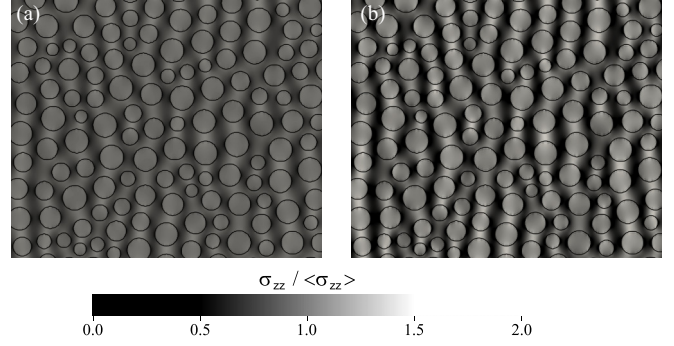


FIG. 7. Magnification of typical  $\sigma_{22}$  stress maps for  $\varphi = 0.396$  and toughness ratio (a)  $\beta = 2.0$ , (b)  $\beta = 10.0$ . The stress is normalized by the mean stress value  $\langle \sigma_{zz} \rangle$ . The gray levels were scaled in order to emphasize the stress concentration zones. As expected, the contrast increases with  $\beta$ .

investigated theoretically by Yevgeny and Lasko [38]. Using this model the stress concentration factor in tension

$$K_\beta \equiv \frac{3\beta}{2\beta + 1} \simeq \frac{\sigma_{\max}}{\sigma} \quad (10)$$

is reached in the vicinity of both particle poles (see Appendix A) where  $K_\beta$  is identified to  $\simeq k_z$  determined for a single particle in tension).  $K_\beta$  is an increasing monotonic function of  $\beta$  varying in a finite interval from 1–1.5 for  $\beta = 1.0$  (corresponding to a homogeneous material) and  $\beta = \infty$  (for a perfectly rigid inclusion), respectively. Interestingly, this value does not depend on the size of the particle.

At high particle volume fractions  $\varphi$  elastic interactions occur between neighboring inclusions (Fig. 7). These interactions lead to long-ranged correlations in the stress field and result in stress patterns similar to force chains already observed in dry [39,40] and cemented [10] granular materials.

To elucidate the influence of  $\varphi$  on stress transmission, we investigate the role of pairwise stress concentration between neighboring inclusions. It is clear that the stress concentration decreases with particle dilution and more precisely with the size of the gaps between the particles. A criterion is needed to distinguish particles that are close enough to be involved in pairwise elastic interactions. Two particles are considered as neighbors if  $L < \lambda(R_i + R_j)$ , where  $L$  is the distance between the centers of particle,  $R_i$  and  $R_j$  are the radii of  $i$  and  $j$  before shrinking, respectively, and  $\lambda = 1.1$  in our simulations [Fig. 8(a)].

After the shrinking of particles, we get a composite material where the gap  $\Delta = L - \alpha R_i - \alpha R_j$  [Fig. 8(b)]. These active gaps constitute a lattice through which the largest stresses are transmitted from the boundary conditions [Fig. 8(c)].

Using the average radius  $R_{\text{eff}} = (R_i + R_j)/2$  we define  $\bar{\Delta} = \Delta/\alpha R_{\text{eff}}$  the normalized gap. If  $R$  is of the order of magnitude of the average particle radius, a typical value of the gap is  $\Delta = 2(R - \alpha R)$ , and  $\bar{\Delta} = 2(1 - \alpha)/\alpha = 2(1/\alpha - 1)$ . Noting that  $\varphi = \alpha^2 \varphi^c$  we get  $1/\alpha = \sqrt{\varphi^c/\varphi}$  and

$$\bar{\Delta} = 2 \left( \sqrt{\frac{\varphi^c}{\varphi}} - 1 \right). \quad (11)$$

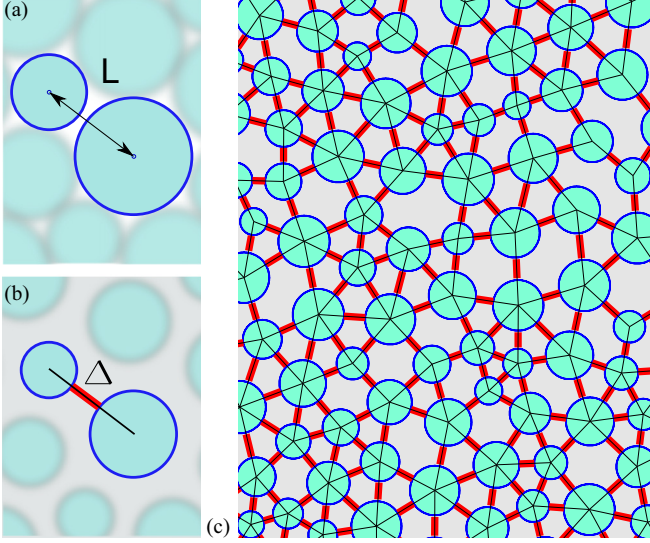


FIG. 8. Gaps between neighboring inclusions. (a) Neighboring particles in the initial granular packing. The distance between particle centers is  $L$ . (b) Shrunken inclusions in the final composite material,  $\Delta$  is the gap between the surface of particles. (c) A typical lattice of gaps between neighboring particles ( $\varphi = 0.396$ ). The inclusions are shown in blue color, the matrix is in light grey, a thin black line is drawn between neighboring particles and gaps are thick red lines.

Figure 9 shows that this model is in good agreement with the numerical computation of  $\langle \bar{\Delta} \rangle$ . It is worth noting that this univocal relationship between  $\langle \bar{\Delta} \rangle$  and  $\varphi$  is clearly a consequence of the sample building procedure. Other procedures such as Monte Carlo [14] or fast Poisson sampling [22] would lead to different relationships. As expected,  $\langle \bar{\Delta} \rangle$  decreases with  $\varphi$  and for  $\alpha = 1.0$ , the mean gap vanishes when the particle fraction reaches the critical value  $\varphi^c = 0.754$ .

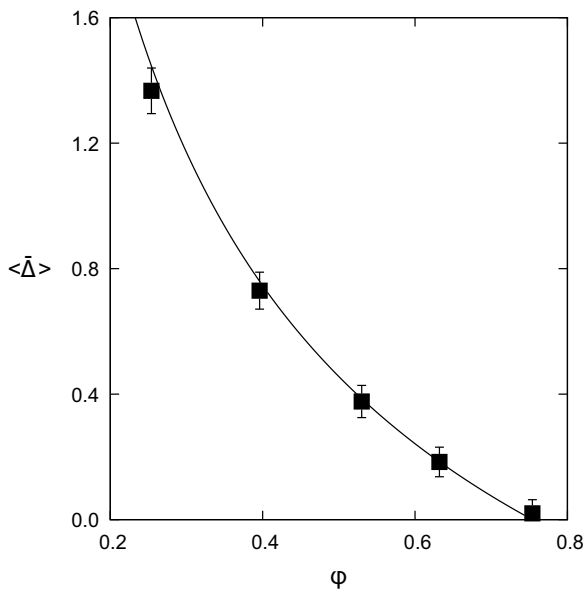


FIG. 9. Average value of the normalized gaps  $\bar{\Delta}$  as a function of particle fraction  $\varphi$ . Error bars are standard deviations. The solid curve is Eq. (11).

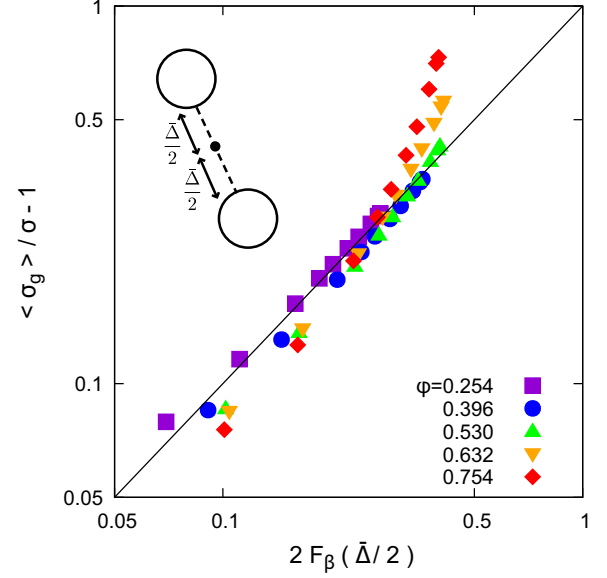


FIG. 10. Normalized average stress in gaps  $\langle \sigma_g \rangle / \sigma$  from numerical simulations as a function of  $2F_\beta(\bar{\Delta}/2)$  for various values of particle fraction  $\varphi$ . The geometrical factor is set to  $A = 0.4$ . The solid straight line is the identity function. Inset: for a pair of particles, the black dot indicates the position where  $\sigma_g$  is evaluated.

It has to be underlined that in this framework the loading direction is not taken into account. A consequence is that all gaps contribute equally independently to their orientation and contribution to stress transmission. The validity of this approximation relies on the fact that the material is isotropic.

For each gap, we consider  $\sigma_g = \sigma \cdot \mathbf{n}$  the normal stress in the middle of the gap, where  $\sigma$  is the stress tensor and  $\mathbf{n}$  is the unit branch vector. In order to provide a theoretical evaluation of  $\langle \sigma_g \rangle / \sigma$ , let us consider the stress distribution in the gap between a pair of identical inclusions placed one above the other. Assuming that the principle of superposition holds, the stress is the sum of three terms: the mean stress  $\sigma$  and the elastic stress induced by each inclusion taken independently. Both last two terms can be evaluated using Eq. (A4) (see Appendix A) by disregarding the mean-field term. By denoting  $\delta$  the distance from the boundary of the considered inclusion ( $\delta \in [0, \bar{\Delta}]$ ) we get

$$F_\beta(\delta) = \frac{A}{2}(K_\beta - 1) \left[ 5 - \frac{3}{u^2(\delta)} \right] \frac{1}{u^2(\delta)}, \quad (12)$$

where  $u(\delta) = 1 + \delta$  and  $A$  is a geometrical factor reflecting the distribution of gap orientations in the sample.

As  $\langle \sigma_g \rangle / \sigma$  is evaluated for both inclusions in the middle of the gap ( $\delta = \bar{\Delta}/2$ ) the two elastic terms are identical and

$$\frac{\langle \sigma_g \rangle}{\sigma} - 1 \simeq 2F_\beta \left( \frac{\bar{\Delta}}{2} \right). \quad (13)$$

Figure 10 shows that for  $A = 0.4$  we get a good agreement between  $\langle \sigma_g \rangle / \sigma$  and the theoretical model [Eq. (13)]. While for diluted cases ( $\varphi < 0.4$ ) data collapses on a straight line regardless of the values of  $\beta$ , in the densest cases ( $\varphi > 0.6$ ) a second regime occurs at high  $\beta$  values. Interestingly this

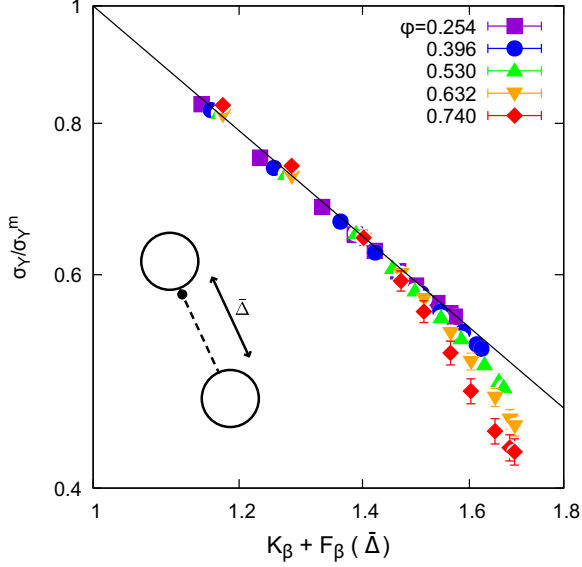


FIG. 11. Normalized mean yield stress  $\langle\sigma_Y\rangle/\sigma_Y^m$  as a function of  $K_\beta + F_\beta(\bar{\Delta})$ . The solid line is a power law with exponent  $\gamma = -1.3$ . Inset: The black dot indicates the position where the stress concentration is evaluated (assuming that failure will occur at this point).

latter is concomitant with the appearance of percolating stress chains in the sample.

In the following, we will investigate the influence of elastic interactions on yield stress. We will also study the statistical distribution of these yield stress for large sets of samples broken in tension.

### C. Yield stress

In Sec. IV B, we proposed a theoretical evaluation of the average stress in the middle of the gaps  $\langle\sigma_g\rangle$ . However, the failure occurs in the close vicinity of the grains. The stress concentration at the origin of crack initiation must be evaluated at this level. If we consider the case of two particles embedded into a matrix, the maximal stress concentration will occur close to one of the two particles. According to Eq. (12) and the principle of superposition, the maximum stress concentration is the sum of the stress induced by this closest inclusion and that induced by the farthest one.

The first contribution is approximatively equal to  $K_\beta$  and the second one is  $F_\beta(\bar{\Delta})$ , obtained using Eq. (12). Thus, as a first approximation

$$\frac{\langle\sigma_Y\rangle}{\sigma_Y^m} \simeq [K_\beta + F_\beta(\bar{\Delta})]^{-\gamma}, \quad (14)$$

where  $\gamma$  is expected to be positive.

While the expression of  $K_\beta$  is purely theoretical, the expression of  $F_\beta(\bar{\Delta})$  depends on  $A$ , which is a geometric parameter accounting for the microstructure. Since  $F_\beta(\bar{\Delta})$  is used to evaluate long-range interactions between inclusions, it seems reasonable, as a first approximation, to adjust the value of  $A$  by considering the middle of the gap, where long-range interactions are dominant.

Figure 11 shows that this approximation (with  $\gamma = 1.3$ ) is in good agreement with the data from the numerical

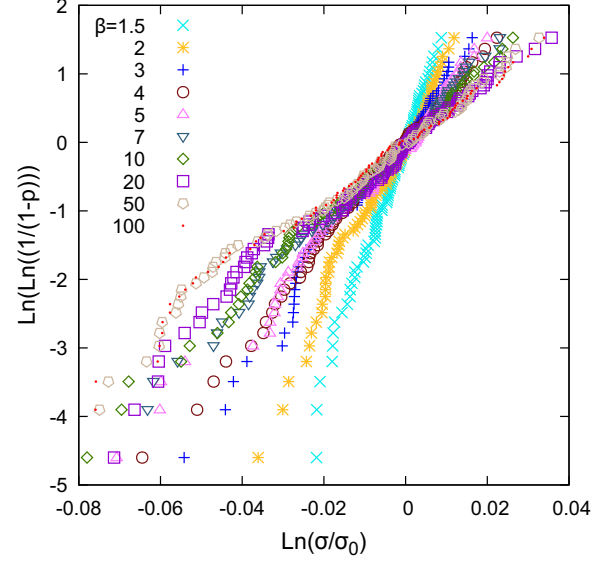


FIG. 12. Cumulative probability of failure  $p$  as a function of the applied stress  $\sigma$  for  $\phi = 0.530$  and various values of  $\beta$ . In order to gather all curves, for each  $\beta$  the stress is normalized by its corresponding value of  $\sigma_0$ .

simulations except for large stress concentrations [ $K_\beta + F_\beta(\bar{\Delta}) > 1.5$ ]. Interestingly, the deviation of the plot from the power law occurs at stress concentrations where stress chains start to appear.

### D. Statistical analysis of failure

In this section, we investigate the statistical distribution of yield stresses for large sets of tensile tests. The probability  $p$  for a sample to break under a stress  $\sigma$  increases with  $\sigma$ . Although for a perfectly homogeneous isotropic material, the distribution has a very narrow span (as there is only one yield stress value  $\sigma_Y$ ) it is generally not the case for usual particle embed composites whose inclusions act as random heterogeneities. In other words, the span of the distribution is a signature of the possible variability of the microstructure.

Following the work of Weibull [41] we considered the cumulated probability  $p$  of failure of a sample submitted to a given stress  $\sigma$  (in a tensile experiment). To fit the data we used the so-called Weibull law

$$p = 1 - e^{-(\sigma/\sigma_0)^m}, \quad (15)$$

where  $\sigma_0$  is a scale factor corresponding to the stress for which 63.2% of samples are broken and  $m$  is the Weibull modulus characterizing the span of the distribution. Note that  $\sigma_0$  is not independent of  $\langle\sigma_Y\rangle$ , as  $\langle\sigma_Y\rangle = \int_0^\infty \frac{\partial p}{\partial \sigma} \sigma d\sigma$ . After a few calculations, we get  $\langle\sigma_Y\rangle = \sigma_0 \Gamma(1 + 1/m)$ , where  $\Gamma$  is the gamma function.

It is classical to use  $\text{Ln}(\sigma)$  and  $\text{Ln}(\text{Ln}(1/(1-p)))$  axis in which Eq. (15) appears as straight line. As an example for  $\phi = 0.530$ , Fig. 12 shows that for each value of  $\beta$  the points follow an almost straight line except at low yield stresses where they deviate from the main linear trend. We also observe that the slope  $m$  decreases with  $\beta$ , showing that heterogeneities

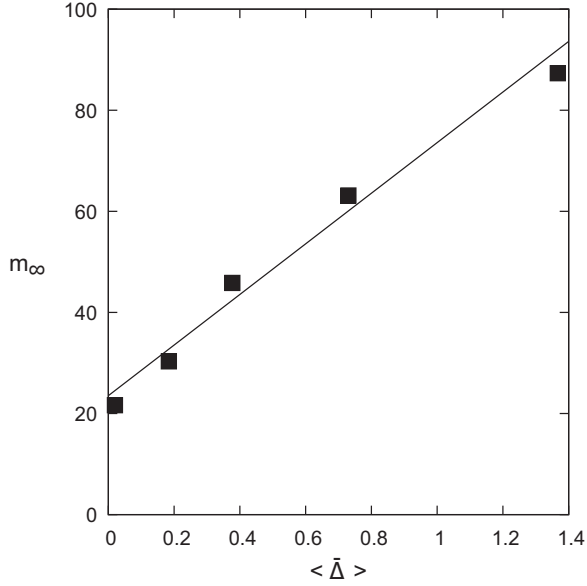


FIG. 13. Weibull modulus  $m_\infty$  for perfectly rigid particles (calculated with  $\beta = 100$  values) as a function of  $\langle \bar{\Delta} \rangle$ . Straight line is Eq. (16).

in stress concentrations lead to a larger dispersion of yield stresses.

In order to investigate the relationship between the Weibull modulus and  $\beta$  and  $\varphi$  we first note that at high  $\beta$  values the slope  $m$  tends to converge toward a finite value  $m_\infty$  corresponding to the case of perfectly rigid inclusions (note that in this study we consider that  $m_\infty$  is obtained for  $\beta = 100$ ).

For the range of  $\langle \bar{\Delta} \rangle$  of our experiments, Fig. 13 shows that  $m_\infty$  can be approximated by a straight line:

$$m_\infty = m_\infty^c + \kappa_\infty \langle \bar{\Delta} \rangle, \quad (16)$$

where  $m_\infty^c = 23.5$  (for touching particles) and  $\kappa_\infty = 8.61$ . As expected, the Weibull modulus is minimal in the granular regime corresponding to the highest stress heterogeneity in the system.

When the normalized average gap  $\langle \bar{\Delta} \rangle = 0$ , inclusions are almost in contact ( $\varphi = \varphi^c$ ) and the stress concentration reaches its highest magnitude. In this case, the failure stress distribution is broader, and  $m_\infty$  reaches its lowest value (Fig. 13). On the contrary, when  $\langle \bar{\Delta} \rangle$  increases, the stress concentration decreases. Concurrently, the yield stress dispersion gets smaller, and  $m_\infty$  increases. According to our model, in the case of an infinite dilution of inclusions, the Weibull modulus is infinite indicating that all samples' yield stress is identical (without any dispersion). In this asymptotic case, the yield stress  $\sigma_Y$  tends to  $\sigma_Y^m/K_\beta$ , the distribution becomes a Dirac and  $m$  becomes infinite. This is true whatever  $\beta$  value and thus it remains the case when  $\beta \rightarrow \infty$ . Consequently  $m_\infty \rightarrow \infty$  at the limit of infinitely diluted particles.

Although for rigid particles the Weibull modulus is solely controlled by the spatial distribution of inclusions, in the soft case the influence of  $\beta$  should be taken into account. A simple approach is to express  $m$  as a product of  $m_\infty$  by a function of stress concentration factor  $K_\beta$ . A first constraint is that  $m/m_\infty$  should tend toward 1 when  $\beta$  tends to  $\infty$ . Another constraint is

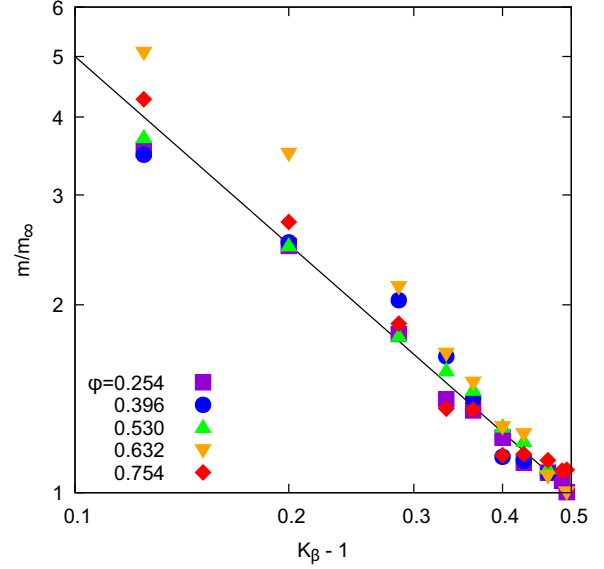


FIG. 14. Normalized Weibull modulus  $m/m_\infty$  as a function of  $K_\beta$  for various values of  $\varphi$ . Straight line is Eq. (17).

that  $m/m_\infty$  should tend to  $\infty$  when  $\beta$  tends to 1. The simplest equation that meets these two conditions is

$$\frac{m}{m_\infty} = \frac{1}{2}(K_\beta - 1)^{-1}. \quad (17)$$

Interestingly, we found a very good agreement between this model and our numerical results (Fig. 14). We note that the data dispersion is higher when  $\beta$  is close to 1.0 (corresponding to the values of  $K_\beta - 1$  close to 0).

## V. CONCLUSION

Using a bond-based peridynamics approach in quasistatic conditions, we investigated the tensile strength, rupture, and probability of failure of dense suspensions of particles embedded in a matrix. By means of DEM simulations, we first simulate slightly polydisperse jammed packing of disks. By applying a uniform shrinkage factor to each disk, these packings were then used to get diluted microstructures. Using this procedure, we randomly generate 100 different phase distribution maps per dilution. These maps were used for the meshing of peridynamics samples. Regarding mechanical parameters, for each sample, we considered ten possible toughness ratios between particle and matrix phases. Finally, a total of 5000 tensile tests were carried out up to failure and analyzed in this paper.

An important issue was to clarify the link between bulk behavior and the spatial distribution of particles. Using a simple expression of the shape factor parameter, we showed that the Halpin-Tsai model is able to fit all Young moduli even for nearly in-contact particles. We showed that the stress distribution between neighboring particles can be approximated using a theoretical function of a stress concentration  $K_\beta$  (which depends on the toughness ratio) and the average size of the gaps between inclusions. We found that, regardless of the particle volume fraction, the fracture is initiated by stress concentrations at the grain scale and the yield stress is a



power law of the local stress concentration. Furthermore, we found that the Weibull modulus, normalized by its value for infinitely rigid particles, is inversely proportional to a function of  $K_\beta$ . In future work, it would be interesting to specify the influence of possible scaling effects on the Weibull modulus. This can be achieved by considering different sample sizes.

Finally, for 2D brittle-elastic suspensions of disk-shaped particles, we were able to propose physically based behavior laws relating the inclusion scale to the global scale. Although the dilution by shrinking leads to convincing samples where the particles are well distributed in the matrix, the obtained behavior laws may strongly depend on this procedure (especially for Yield stresses and Weibull moduli). Indeed, particle disorder is directly inherited from initial granular packings. In future work, we would like to enrich this study by characterizing other types of disorders and assessing to what extent the relationships found deviate from the case of shrinkage dilution. For example, one interesting line of research could be to impose a random fluctuation of particle position. It can also be noted that the present study is limited to  $\beta > 1$ , which corresponds to most situations encountered in practice. In future work, we would like to extend our parametric study on particle-reinforced materials by considering the case of particles that are weaker than the matrix ( $\beta < 1$ ), up to the limit of porous materials ( $\beta \rightarrow 0$ ).

**ACKNOWLEDGMENTS**

We are grateful to the INRAE MIGALE bioinformatics facility [42], to the Genotoul bioinformatics platform Toulouse Occitanie [43], and MESO@LR-Platform at the University of Montpellier, for providing computing and storage resources.

**APPENDIX: STRESS FIELD INDUCED BY A CIRCULAR INCLUSION**

Kirsch [44] proposed a continuum formulation for the stress concentration induced by a circular hole in an infinite elastic plane of elastic parameters  $(E^m, \nu^m)$  submitted to uniaxial loading. The case of an elastic circular inclusion of elastic parameters  $(E^p, \nu^p)$  was investigated by Yevgeny and Lasko [38] who considered that the stress field can be obtained by combining three uniaxial loadings using the superposition principles valid for linear systems. In our case, the solution is the sum of these of a homogeneous stress field, and two solutions of Kirsch in tension and compression applied along the principal axis of the domain. We consider a homogeneous stress  $\langle \sigma_{zz} \rangle$  applied to the domain in  $z$  direction. Denoting

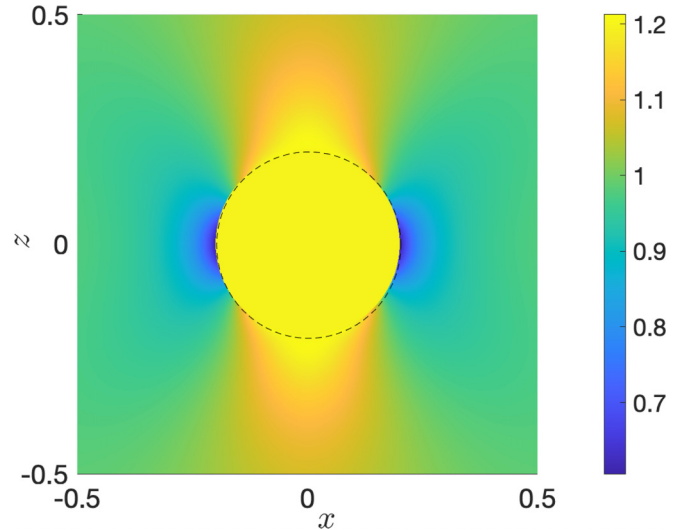


FIG. 15. Stress field  $\sigma_{zz}/\langle \sigma_{zz} \rangle$  induced by a disk-shaped inclusion ( $\beta = 10$ ) for a vertical loading.

$r = \sqrt{x^2 + z^2}$  the radial position, we get in Cartesian coordinates

$$\frac{\sigma_{zz}}{\langle \sigma_{zz} \rangle} = k_z \tag{A1}$$

for  $r < R$  (inside the inclusion) and,

$$\frac{\sigma_{zz}}{\langle \sigma_{zz} \rangle} = 1 + a \left[ 1 + \frac{3R^2 + 10z^2}{r^2} - b + c \right] - \frac{k_x R^2}{r^2} \left( 1 - \frac{2z^2}{r^2} \right) \tag{A2}$$

for  $r \geq R$  (outside the inclusion), where

$$a = \frac{(1-k_z+k_x)R^2}{2r^2}, b = 8z^2 \frac{3R^2+2z^2}{r^4}, c = \frac{24R^2z^4}{r^6} \text{ and}$$

$$k_x = \frac{E^p[(3\nu^p - 1)E^m + (1 - 3\nu^m)E^p]}{(E^m + 2E^p)^2 - [\nu^p E^m + (1 - \nu^m)E^p]^2}$$

$$k_z = \frac{E^p[(3 - \nu^p)E^m + (5 + \nu^m)E^p]}{(E^m + 2E^p)^2 - [\nu^p E^m + (1 - \nu^m)E^p]^2} \tag{A3}$$

In our paper as we considered  $\nu^p = \nu^m = 1/3$ , we get  $k_x = 0$  and  $k_z = 3\beta/(2\beta + 1)$ . By denoting  $u = \frac{z}{R}$  Eq. (A2) becomes

$$\frac{\sigma_{zz}}{\langle \sigma_{zz} \rangle} = 1 + \frac{1}{2}(k_z - 1) \frac{1}{u^2} \left[ 5 - \frac{3}{u^2} \right]. \tag{A4}$$

Figure 15 shows a snapshot of the vertical stress field. The maximum stress concentration  $\frac{\sigma_{zz}}{\langle \sigma_{zz} \rangle} = 1 + (k_z - 1) \frac{25}{24}$  is reached in the vicinity of the poles at  $u = \pm \sqrt{\frac{6}{5}} \simeq 1.1$ . Note that since  $\frac{25}{24} \simeq 1.04$  is close to one  $\frac{\sigma_{zz}}{\langle \sigma_{zz} \rangle} \simeq k_z$ .

[1] H. Van Damme, *Cem. Concr. Res.* **112**, 5 (2018).  
 [2] I. Jebalia, J.-E. Maigret, A.-L. Réguerre, B. Novalés, S. Guessasma, D. Lourdin, G. Della Valle, and M. Kristiawan, *Carbohydr. Polym.* **223**, 115086 (2019).  
 [3] I. Boudina, E. Rondet, S. Nezamabadi, and T. Sharkawi, *Powder Technol.* **397**, 117083 (2022).  
 [4] C. Janssen, F. Wagner, A. Zang, and G. Dresen, *Int. J. Earth Sci.* **90**, 46 (2001).

[5] A. van Grootel, J. Chang, B. L. Wardle, and E. Olivetti, *J. Cleaner Prod.* **261**, 121087 (2020).  
 [6] E. H.-J. Kim, V. K. Corrigan, A. J. Wilson, I. R. Waters, D. I. Hedderley, and M. P. Morgenstern, *J. Texture Stud.* **43**, 49 (2012).  
 [7] M. De Stefano, M. Tanganelli, and S. Viti, *Bull. Earthquake Eng.* **11**, 1711 (2013).  
 [8] V. Topin, F. Radjaï, J.-Y. Delenne, A. Sadoudi, and F. Mabilbe, *J. Cereal Sci.* **47**, 347 (2008).

- [9] V. Topin, J.-Y. Delenne, F. Radjai, L. Brendel, and F. Mabilie, *Eur. Phys. J. E* **23**, 413 (2007).
- [10] X. Frank, F. Radjai, S. Nezamabadi, and J.-Y. Delenne, *Phys. Rev. E* **102**, 022906 (2020).
- [11] D. Arencón and J. I. Velasco, *Materials* **2**, 2046 (2009).
- [12] S. R. Bakshi, D. Lahiri, and A. Agarwal, *Int. Mater. Rev.* **55**, 41 (2010).
- [13] Q. T. Shubhra, A. M. Alam, and M. A. Quaiyyum, *J. Thermoplast. Compos. Mater.* **26**, 362 (2013).
- [14] H. Laubie, F. Radjai, R. Pellenq, and F.-J. Ulm, *Phys. Rev. Lett.* **119**, 075501 (2017).
- [15] C. Ye, J. Shi, and G. J. Cheng, *Int. J. Fatigue* **44**, 151 (2012).
- [16] S. A. Ponnusami, S. Turteltaub, and S. van der Zwaag, *Eng. Fract. Mech.* **149**, 170 (2015).
- [17] T. T. Nguyen, J. Yvonnet, Q.-Z. Zhu, M. Bornert, and C. Chateau, *Eng. Fract. Mech.* **139**, 18 (2015).
- [18] V. Chiaruttini, D. Geoffroy, V. Riolo, and M. Bonnet, *Eur. J. Comput. Mech.* **21**, 208 (2012).
- [19] R. Affès, J.-Y. Delenne, Y. Monerie, F. Radjai, and V. Topin, *Eur. Phys. J. E* **35**, 117 (2012).
- [20] S. A. Silling, *J. Mech. Phys. Solids* **48**, 175 (2000).
- [21] S. A. Silling, M. J. Epton, O. Weckner, J. Xu, and E. Askari, *J. Elasticity* **88**, 151 (2007).
- [22] K. Heinze, X. Frank, V. Lullien-Pellerin, M. George, F. Radjai, and J.-Y. Delenne, *Phys. Rev. E* **101**, 052901 (2020).
- [23] Y. D. Ha and F. Bobaru, *Int. J. Fract.* **162**, 229 (2010).
- [24] Y. D. Ha and F. Bobaru, *Eng. Fract. Mech.* **78**, 1156 (2011).
- [25] W. Gerstle, N. Sau, and S. A. Silling, *Nucl. Eng. Design* **237**, 1250 (2007).
- [26] P. Perré, G. Almeida, M. Ayouz, and X. Frank, *Ann. Forest Sci.* **73**, 147 (2016).
- [27] F. Radjai and F. Dubois, *Discrete Numerical Modeling of Granular Materials* (Wiley ISTE, New York, 2011).
- [28] R. Alebrahim, P. Packo, M. Zaccariotto, and U. Galvanetto, *Comput. Part. Mech.* **9**, 597 (2022).
- [29] C. Liu, L. Li, J. Hong, X. Zheng, K. Bian, Y. Sun, and J. Zhang, *Int. J. Food Sci. Technol.* **49**, 253 (2014).
- [30] T. Orellana, E. M. Tejado, C. Funke, W. Fütterer, S. Riepe, H. J. Moller, and J. Y. Pastor, *Int. J. Metall. Mater. Eng.* **1**, 101 (2015).
- [31] O. Buyukozturk and B. Hearing, *Int. J. Solids Struct.* **35**, 4055 (1998).
- [32] M.-Y. He and J. W. Hutchinson, *Int. J. Solids Struct.* **25**, 1053 (1989).
- [33] M. Lebihain, J.-B. Leblond, and L. Ponson, *J. Mech. Phys. Solids* **137**, 103876 (2020).
- [34] G. Hu, G. Guo, and D. Baptiste, *Comput. Mater. Sci.* **9**, 420 (1998).
- [35] R. Hill, *J. Mech. Phys. Solids* **13**, 213 (1965).
- [36] J. H. Affdl and J. Kardos, *Polym. Eng. Sci.* **16**, 344 (1976).
- [37] R. Hewitt and M. De Malherbe, *J. Compos. Mater.* **4**, 280 (1970).
- [38] D. Y. Yevgeny and G. V. Lasko, *Engineering* **04**, 583 (2012).
- [39] F. Radjai, M. Jean, J.-J. Moreau, and S. Roux, *Phys. Rev. Lett.* **77**, 274 (1996).
- [40] T. Majmudar and R. Behringer, *Nature (London)* **435**, 1079 (2005).
- [41] W. Weibull, *J. Appl. Mech.* **18**, 293 (1951).
- [42] MIGALE, INRAE, Migale Bioinformatics Facility, <https://doi.org/10.15454/1.5572390655343293E12>.
- [43] GenoToul Bioinfo, INRAE, GenoToul Bioinformatics Facility, <https://doi.org/10.15454/1.5572369328961167E12>.
- [44] E. G. Kirsh, *Z. Ver. Dtsch. Ing.* **42**, 797 (1898).